Supporting Information for

On the Synthesis of Bi-Magnetic Manganese Ferrite-Based Core-Shell Nanoparticles

Marco Sanna Angotzi,[a,b] Valentina Mameli,[a,b] Claudio Cara,[a,b] Davide Peddis,[b,c,d] Huolin L. Xin,[e] Claudio Sangregorio,[b,f,g] Maria Laura Mercuri,[a] Carla Cannas*[a,b]

[a]Department of Chemical and Geological Sciences, University of Cagliari, S.S. 554 bivio per Sestu, 09042 Monserrato (CA), Italy

[b]Consorzio Interuniversitario Nazionale per la Scienza e Tecnologia dei Materiali (INSTM), Via Giuseppe Giusti 9, 50121 Firenze (FI), Italy

[c]Dipartimento di Chimica e Chimica Industriale, Universit`a di Genova, via Dodecaneso, 31, 16131 Genova, Italy

[d]Istituto di Struttura della Materia, Consiglio Nazionale delle Ricerche, Via Salaria Km 29.300, 00015Monterotondo Scalo (RM), Italy

[e]Department of Physics and Astronomy, University of California, Irvine, CA 92617, USA

[f]Istituto di Chimica dei Composti OrganoMetallici - Consiglio Nazionale delle Ricerche (ICCOM-CNR), Via Madonna del Piano 10, 50019 Sesto Fiorentino (FI), Italy

[g]Department of Chemistry "U. Schiff", University of Florence, Via della Lastruccia 3-13, 50019, Sesto Fiorentino (FI), Italy

Table of Contents

Scheme of the synthesis

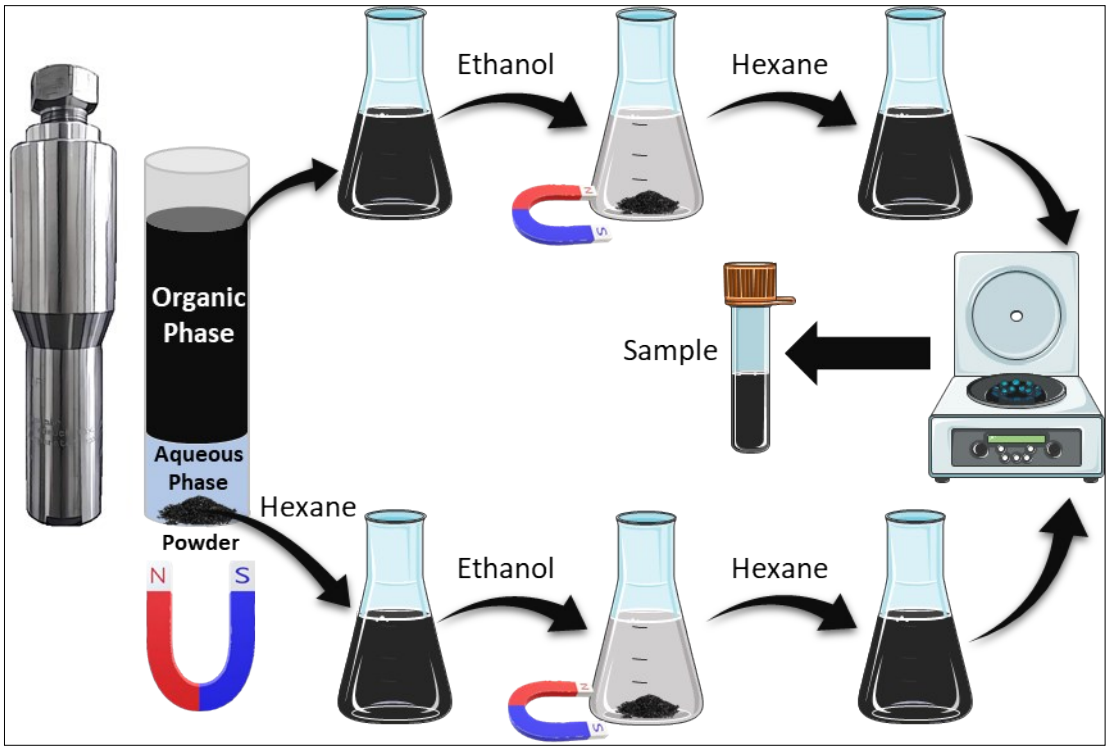

Figure 1S. Scheme of the solvothermal synthesis. All samples were recovered after separation with magnet from the bottom of the Teflon liner, whashing with hexane and ethanol, redispersing in hexane, and centrifugating. The sample MnA@Fe1S was recovered from the organic phase of the mother liquor, after destabilizing the system with ethanol, washing the particles as before, redispersing in hexane, and centrifugating.

Additional measurements of the samples

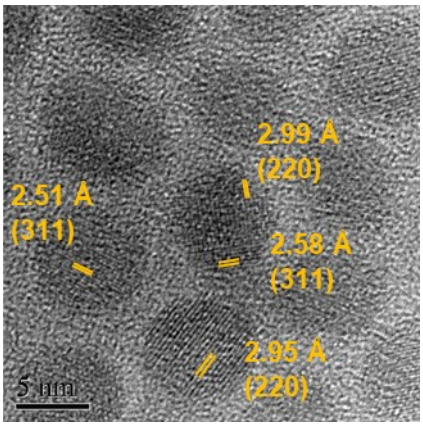

Figure 2S. HRTEM image with inter-lattice distances and Miller's indexes of MnA.

FTIR spectra (Figure 3S) show the main vibrational modes related to the oleate molecule, *i.e.*, the COO^- vibrational modes (ν_{as} COO^-, ν_s COO^- at 1548 and 1421 cm^{-1}, respectively) and those related to the hydrocarbon chain (ν_{as} C-H(CH_3), ν_{as} C-H(CH_2), ν_s C-H(CH_2), ν_s C-H(CH_3), at 3004, 2954, 2921, and 2850 cm^{-1}, respectively). The band at about 570 cm^{-1} are due to the Me-O stretching mode of the tetrahedral and octahedral sites of the spinel structure in the manganese ferrite samples.[70,71] These band is shifted to 580 cm^{-1} for MnA@Co, due to the presence of cobalt ferrite.[71,72] The samples where iron oxide is present, feature, in the region between 700-350 cm^{-1}, the typical bands of maghemite.[10,63]

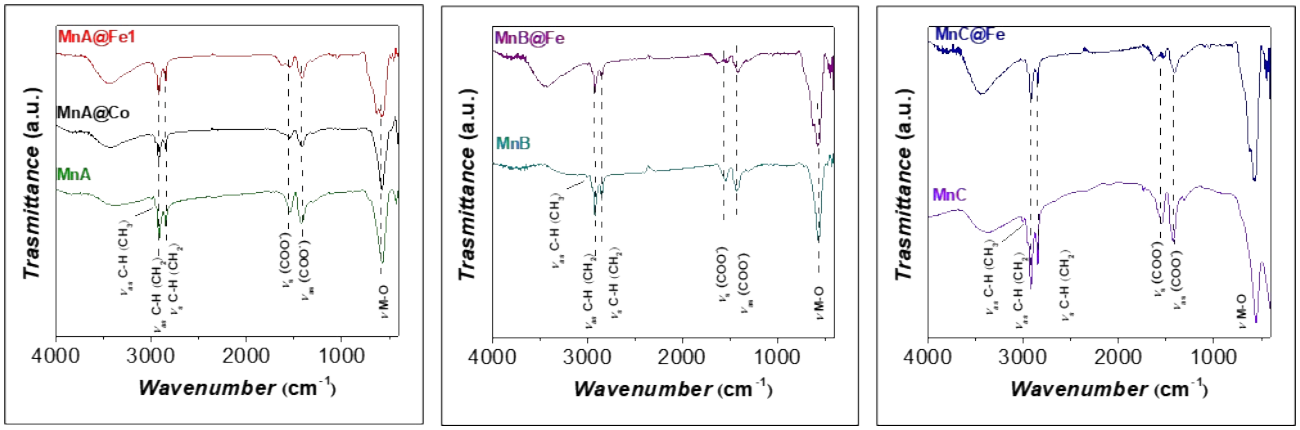

Figure 3S FTIR spectra of the samples

TGA curves (Figure 4S) display a weight loss at about 260-270 °C, correspondent to the oleate decomposition.[10,73] The percentage correspond to a monolayer of capping molecule on the nanoparticles' surface.

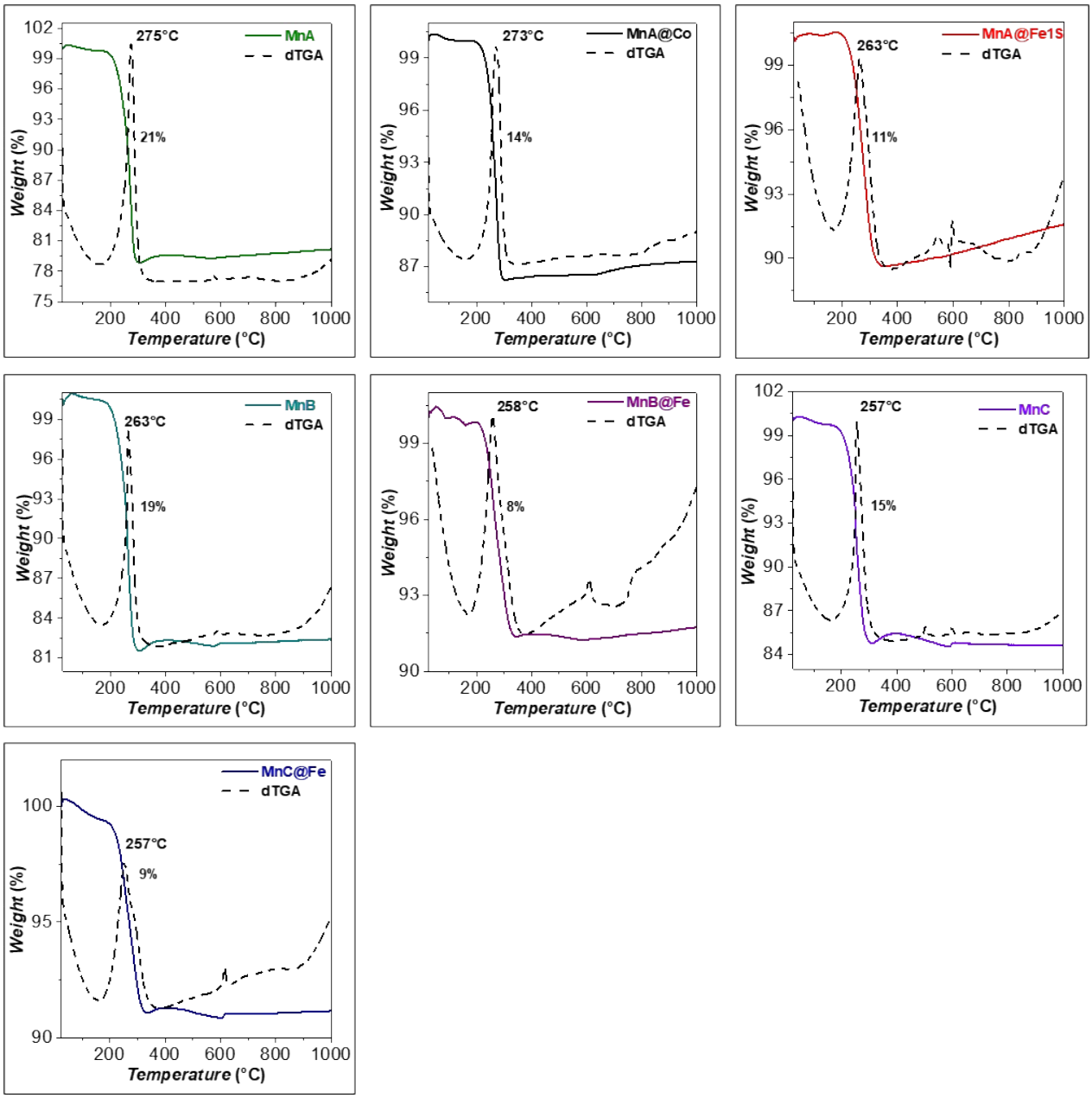

Figure 4S TGA curves of the samples.

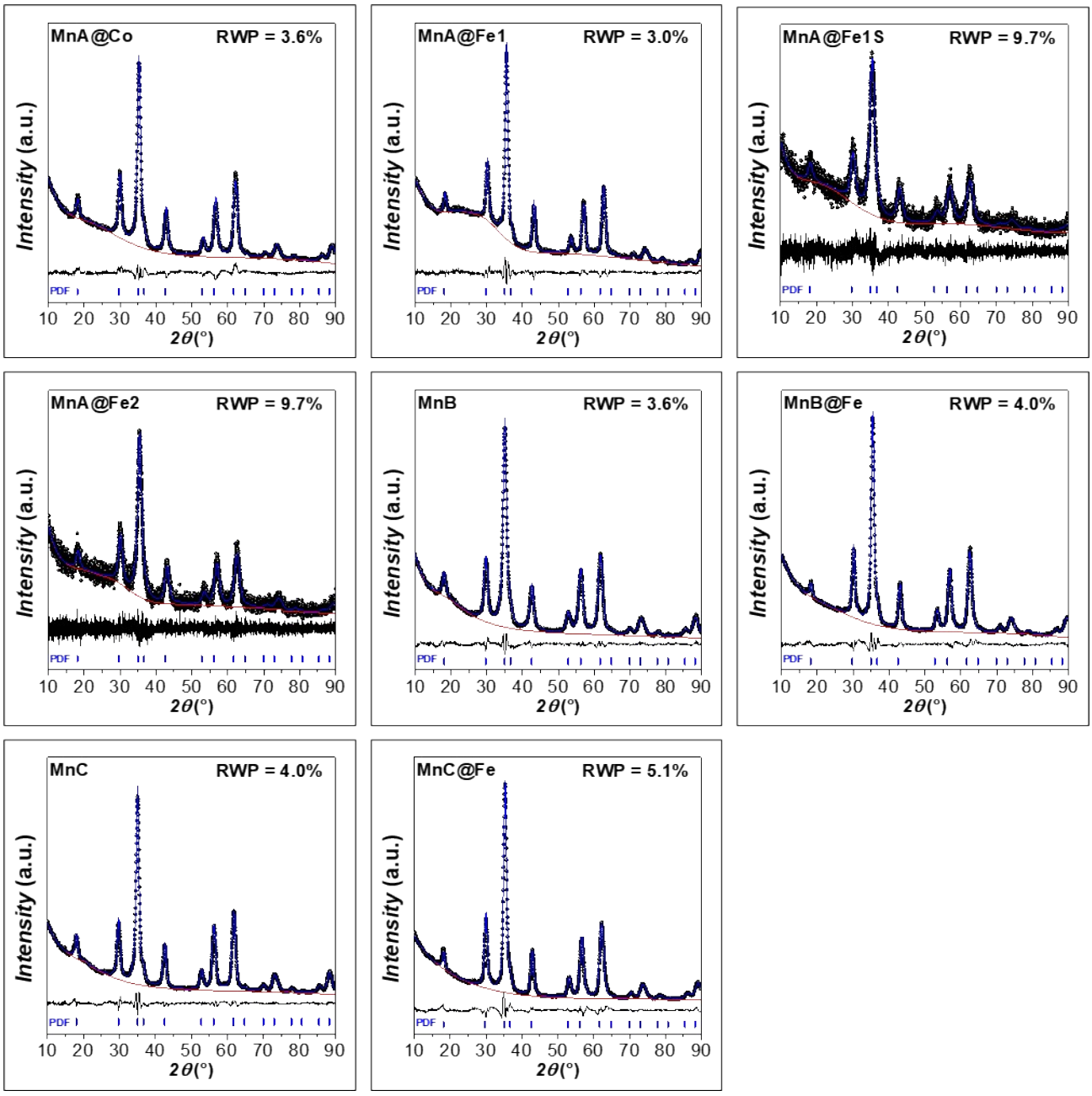

Figure 5S. Rietveld refinements of the XRD patterns of the samples.

Parameters of cations

Table 1S. Reported parameters for the cations. C.N. = coordination number. HS = high spin. LS = low spin.

Cation	Hydratation enthalpies aqua ions[7] (kJ/mol)	K_{ps} hydroxides	Ionic Radius, C.N.4 [8] (pm)	Ionic Radius, C.N.6 HS[8] (pm)	Ionic Radius, C.N.6 LS[8] (pm)
Fe^{III}	-4430	$6.3 \cdot 10^{-38}$	49	64.5	55
Co^{II}	-1996	$2.5 \cdot 10^{-16}$	58	74.5	65
Fe^{II}	-1946	$7.9 \cdot 10^{-15}$	63	78	61
Mn^{II}	-1841	$4.6 \cdot 10^{-14}$	66	83	67

Magnetic properties

Table 2S. Room temperature ^{57}Fe Mössbauer parameters of the samples: values of the isomer shift (δ), hyperfine field (B_{hf}), and full width at half-maximum (FWHM) of the components.

Sample	Signal	Site	δ (mm/s)	B_{hf} (T)	FWHM (mm/s)
MnA	Singlet	-	0.32	-	2.92
MnA@Co	Sextet	T_d	0.30	46.8	0.38
	Sextet	O_h	0.39	44.3	0.98
MnA@Fe1	Singlet	-	0.41	-	2.48
MnA@Fe2	Singlet	-	0.36	-	1.95
Co	Sextet	T_d	0.30	48.1	0.44
	Sextet	O_h	0.36	45.5	0.91

Table 3S. Low temperature ^{57}Fe Mössbauer parameters of the samples: values of the isomer shift (δ), hyperfine field at 0 and 6 Tesla (B_{hf}), relative area (A), spin canting (α), and inversion degree (γ).

Sample	Signal	Site	δ (mm/s)	B_{hf}^{0T} (T)	B_{hf}^{6T} (T)	A (%)	α (°)	γ
MnA	Sextet	T_d	0.45	53.3	59.4	22	0	0.46
	Sextet	O_h	0.56	52.8	47.2	78	18	
MnA@Fe1	Singlet	T_d	0.41	53.2	59.2	37	0	-
	Singlet	O_h	0.55	54.2	48.4	63	15	

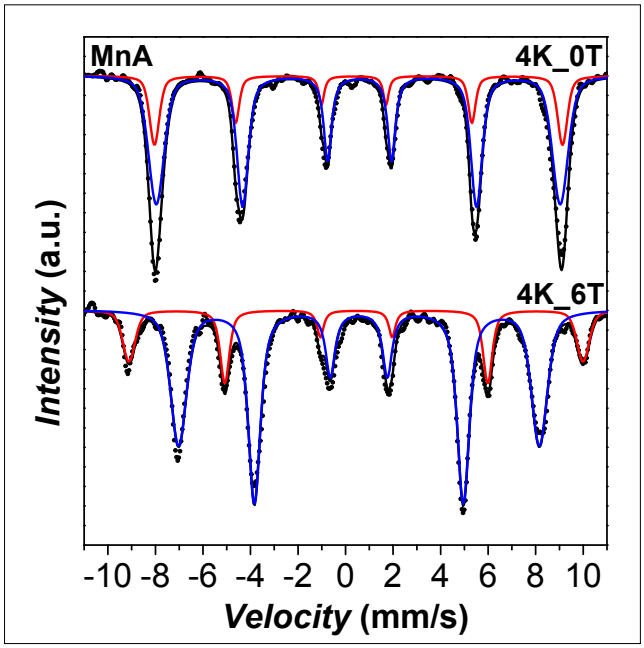

Figure 6S. LT ^{57}Fe Mössbauer spectra of the samples in the presence and in the absence of external magnetic field of the sample MnA

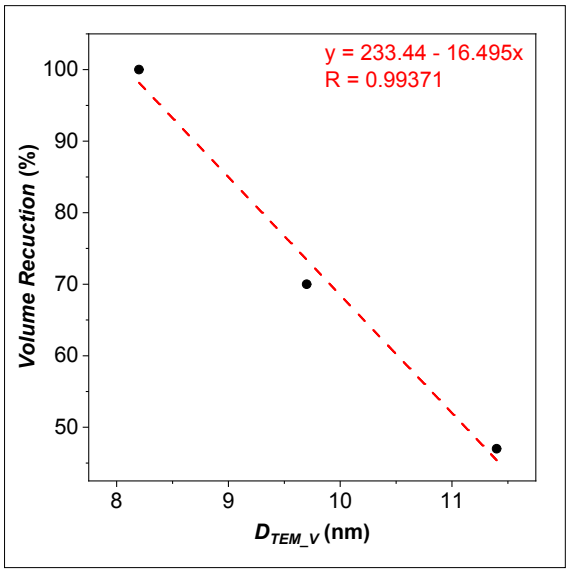

Figure 7S. Linear fit of D_{TEM_V} of manganese ferrite cores vs volume reduction of the cores in the respective core-shell nanoparticles

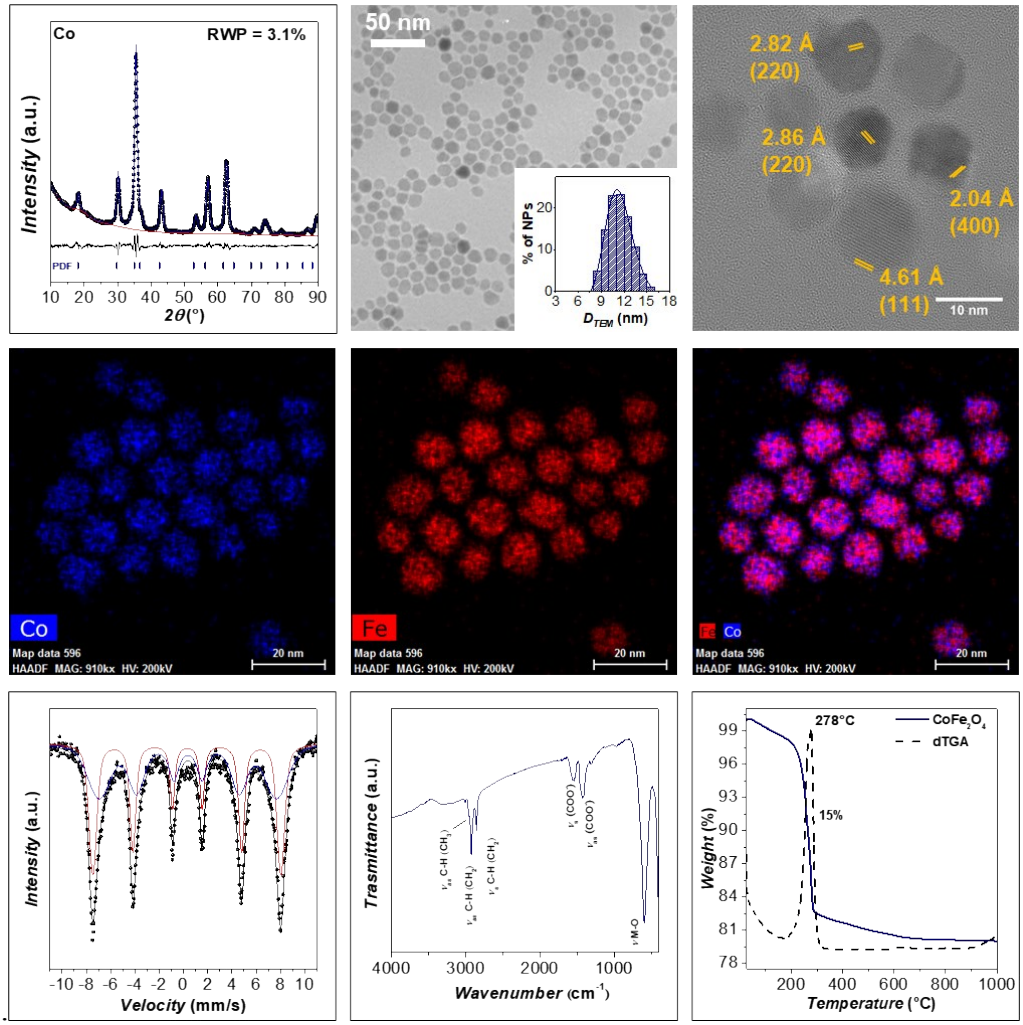

Figure 8S. Rietveld refinement of the XRD pattern, TEM image with size distribution, HRTEM image with interlattice distances and Miller's indexes, STEM-EDX chemical mapping images, RT ^{57}Fe Mössbauer spectrum, FT-IR spectrum, and TGA curve of the Co sample. Particles used for the analysis: 11600.

Considered the higher hyperfine field values of Co than MnA@Co, we can hypothesize a higher anisotropy constant for the cobalt ferrite sample, therefore a slower Néel relaxation time, since $\tau_N = \tau_0 e^{(KV/K_BT)}$. Moreover, DLS analysis (Figure 9S) revealed a hydrodynamic diameter for the single-phase and core-shell samples of 33 nm and 23 nm, respectively, corresponding to 2-3 aggregated particles. The associated Brown relaxation times (τ_B) correspond to $1.1 \cdot 10^{-4}$ for MnA@Co and $1.2 \cdot 10^{-3}$ s for Co. Therefore, both τ_B and τ_N are closer to the characteristic time of the hyperthermic measurement ($\tau_{SAR} = 1/2\pi\nu = 8.7 \times 10^{-7}$ s) for the core-shell sample, explaining the reason behind the increased heating ability.

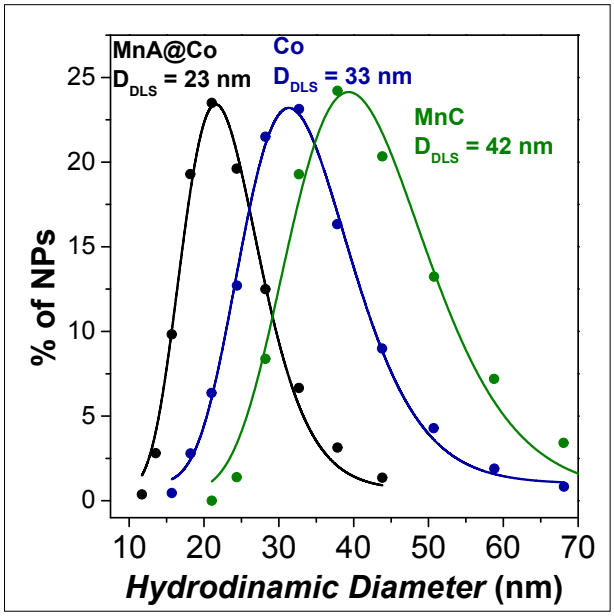

Figure 9S. DLS and curves of the aqueous colloidal dispersions of the samples.

Table 4S. Volume-weight particle size (D_{TEM_V}) and percentage standard deviation (σ), hydrodynamic diameter (D_{DLS}), diffusion coefficient (D), Brown relaxation time (T_B), specific adsorption rate (SAR), and intrinsic loss power (ILP) of the samples MnA@Co and Co.

Sample	D_{TEM_V} (nm)	σ (%)	D_{DLS} (nm)	D (μ^2/s)	τ_B (s)	SAR (W/g_{ox})	ILP (nH·m^2·kg_{ox}^{-1})
MnA@Co	11.6	9	23(6)	7.7	$1.1 \cdot 10^{-4}$	43(5)	0.81(9)
Co	11.7	12	33(8)	3.5	$1.2 \cdot 10^{-3}$	24(1)	0.45(2)
MnC	11.4	13	42(10)	2.6	$3.0 \cdot 10^{-3}$	0	0

Additional STEM-EDX images

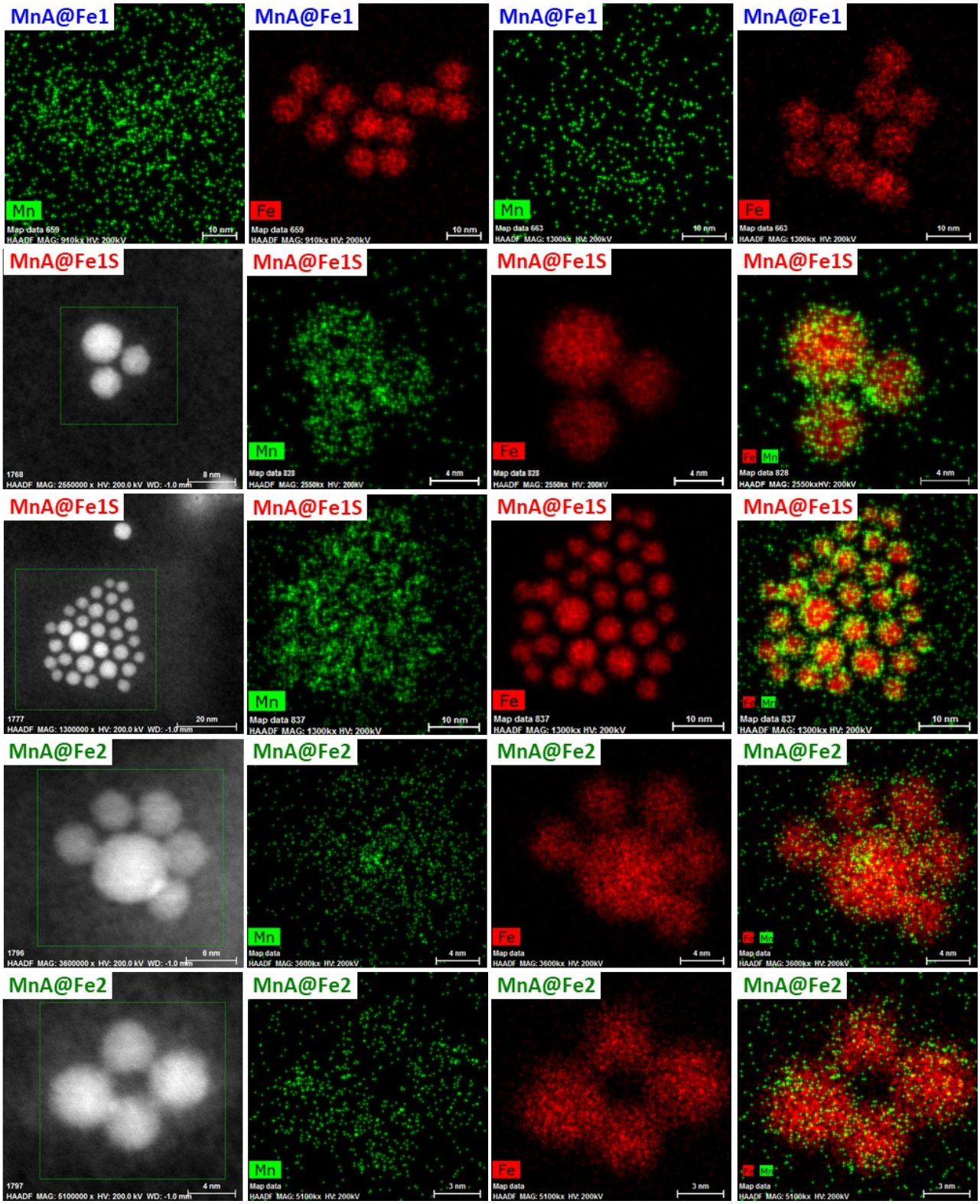

Figure 10S. STEM-EDX chemical mapping of the samples MnA@Fe1, MnA@Fe1S, and MnA@Fe2. Manganese is presented in green, iron in red.

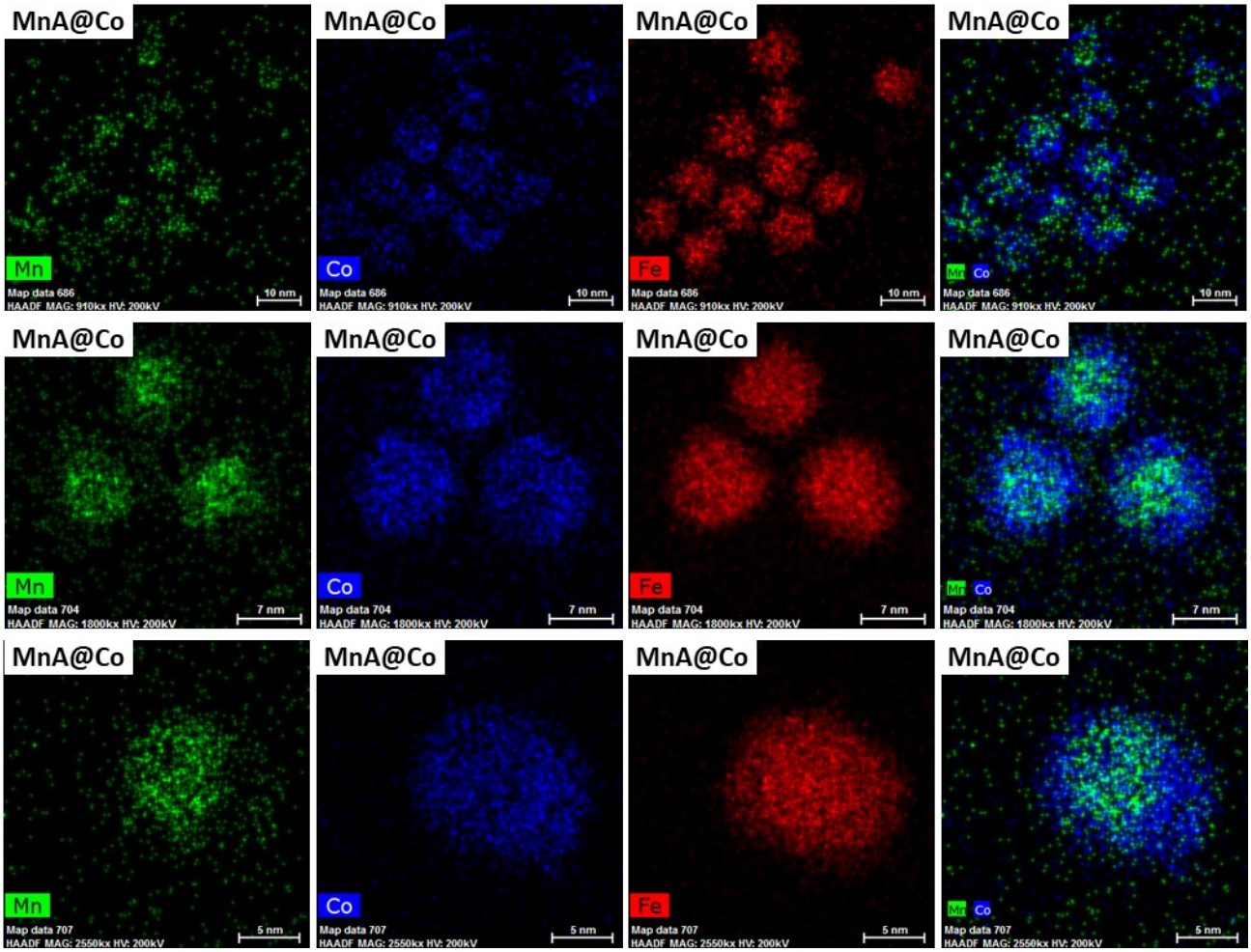

Figure 11S. STEM-EDX chemical mapping of the sample MnA@Co. Cobalt is represented in blue, manganese in green, and iron in red

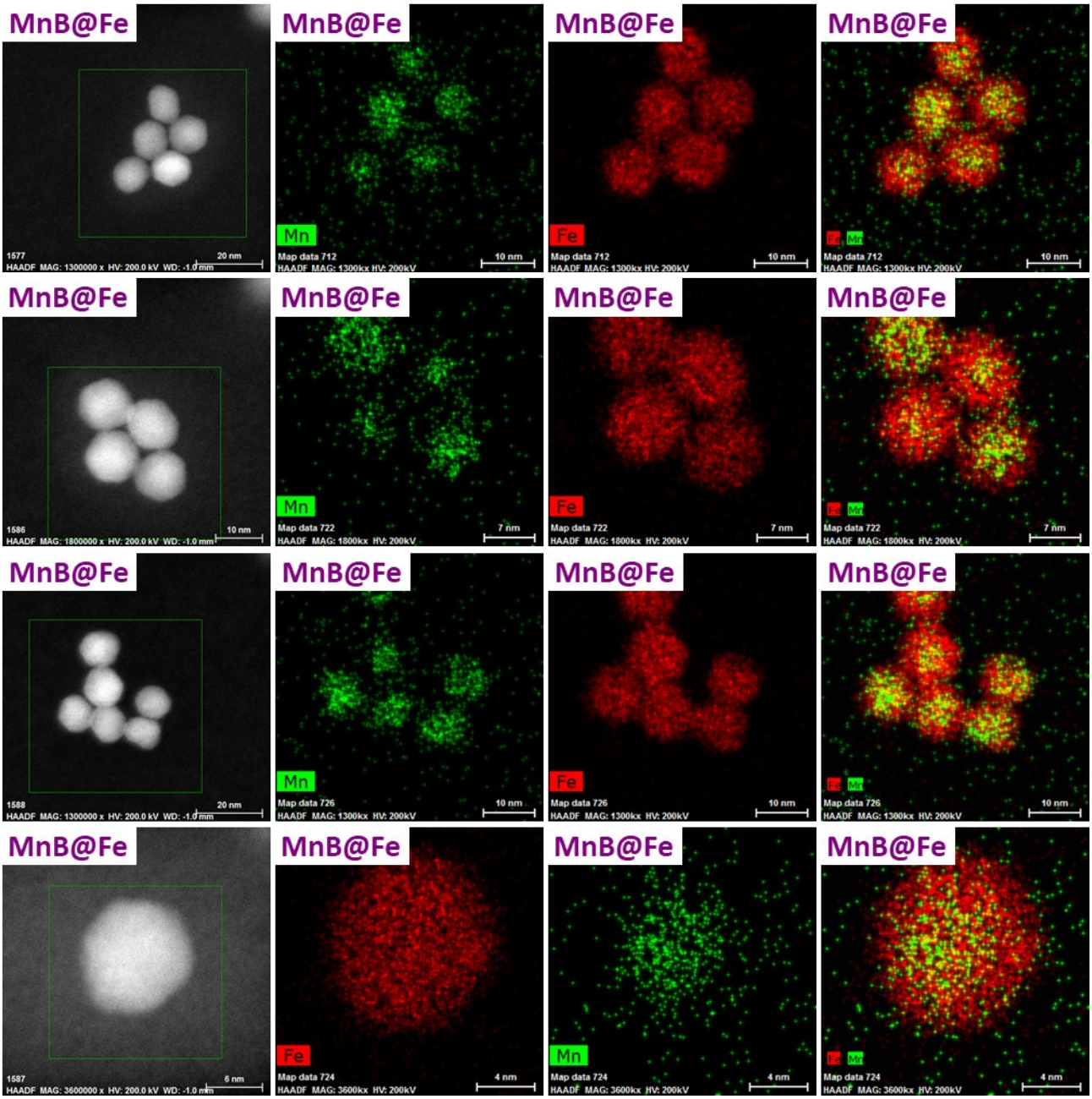

Figure 12S. STEM-EDX chemical mapping of the sample MnB@Fe. Manganese is presented in green, iron in red.

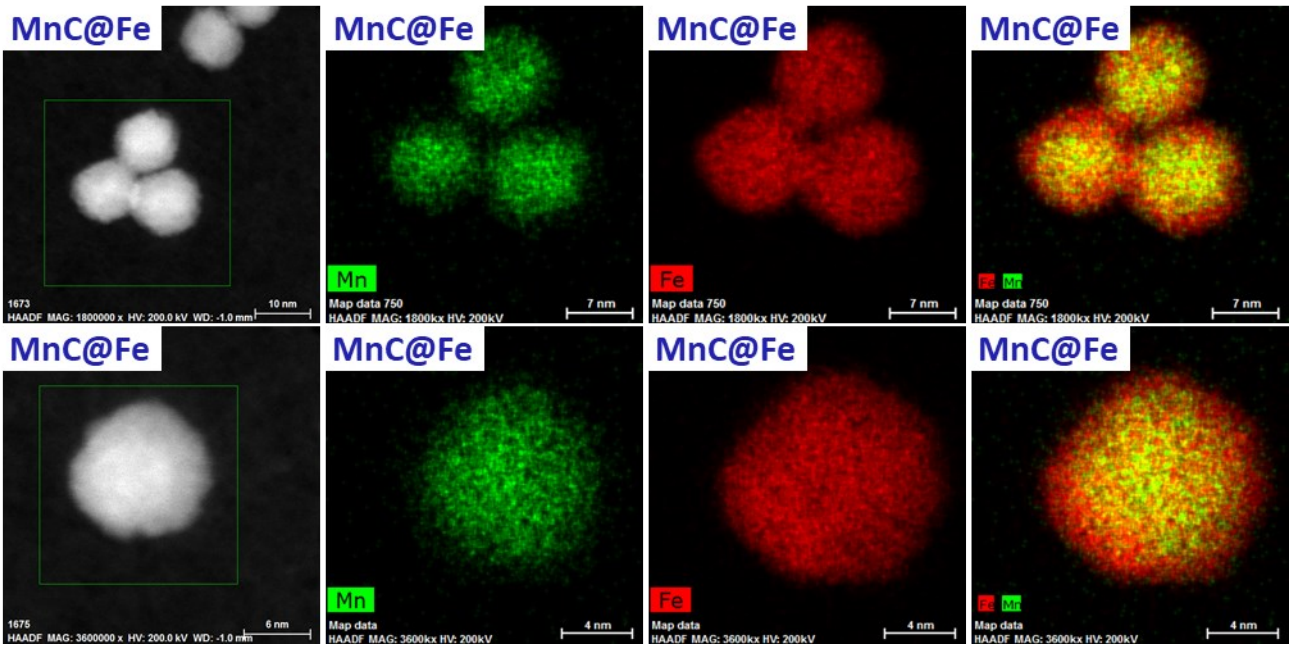

Figure 13S. STEM-EDX chemical mapping of the sample MnC@Fe. Manganese is presented in green, iron in red.

References

(1) Cannas, C.; Musinu, A.; Ardu, A.; Orrù, F.; Peddis, D.; Casu, M.; Sanna, R.; Angius, F.; Diaz, G.; Piccaluga, G.; et al. CoFe2O4 and CoFe2O4/SiO2 Core/Shell Nanoparticles: Magnetic and Spectroscopic Study. *Chem. Mater.* **2010**, *22* (11), 3353–3361. https://doi.org/10.1021/cm903837g.

(2) White, W. B.; DeAngelis, B. a. Interpretation of the Vibrational Spectra of Spinels. *Spectrochim. Acta Part A Mol. Spectrosc.* **1967**, *23* (4), 985–995. https://doi.org/10.1016/0584-8539(67)80023-0.

(3) Taylor, R. M. Maghemite in Soils and Its Origin I. PROPERTIES AND OBSERVATIONS ON SOIL MAGHEMITES. *Clay Miner.* **1974**, *10* (4), 289–298. https://doi.org/10.1180/claymin.1974.010.4.08.

(4) Sanna Angotzi, M.; Mameli, V.; Cara, C.; Ardu, A.; Nizňnanský, D.; Musinu, A. Oleate-Based Solvothermal Approach for Size Control of M II Fe 2 III O 4 (M II ═ Mn II , Fe II) Colloidal Nanoparticles. *J. Nanosci. Nanotechnol.* **2019**, *19* (8), 4954–4963. https://doi.org/10.1166/jnn.2019.16785.

(5) Sanna Angotzi, M.; Musinu, A.; Mameli, V.; Ardu, A.; Cara, C.; Niznansky, D.; Xin, H. L.; Cannas, C. Spinel Ferrite Core–Shell Nanostructures by a Versatile Solvothermal Seed-Mediated Growth Approach and Study of Their Nanointerfaces. *ACS Nano* **2017**, *11* (8), 7889–7900. https://doi.org/10.1021/acsnano.7b02349.

(6) Mameli, V.; Musinu, A.; Ardu, A.; Ennas, G.; Peddis, D.; Niznansky, D.; Sangregorio, C.; Innocenti, C.; Thanh, N. T. K.; Cannas, C. Studying the Effect of Zn-Substitution on the Magnetic and Hyperthermic Properties of Cobalt Ferrite Nanoparticles. *Nanoscale* **2016**, *8* (19), 10124–10137. https://doi.org/10.1039/C6NR01303A.

(7) Halliwell, H. F.; Nyburg, S. C. Enthalpy of Hydration of the Proton. *Trans. Faraday Soc.* **1963**, *59* (iii), 1126–1140. https://doi.org/10.1039/tf9635901126.

(8) Shannon, R. D. Revised Effective Ionic Radii and Systematic Studies of Interatomic Distances in Halides and Chalcogenides. *Acta Crystallogr. Sect. A* **1976**, *32* (5), 751–767. https://doi.org/10.1107/S0567739476001551.

(9) Coey, J. M. D. *Magnetism and Magnetic Materials*; Cambridge University Press: Cambridge, 2009. https://doi.org/10.1016/0160-9327(88)90178-0.

(10) Lee, J.-H.; Jang, J.-T.; Choi, J.-S.; Moon, S. H.; Noh, S.-H.; Kim, J.-G. J.-W. J.-G. J.-W.; Kim, J.-G. J.-W. J.-G. J.-W.; Kim, I.-S.; Park, K. I.; Cheon, J. Exchange-Coupled Magnetic Nanoparticles for Efficient Heat Induction. *Nat. Nanotechnol.* **2011**, *6* (7), 418–422. https://doi.org/10.1038/nnano.2011.95.

(11) Sanna Angotzi, M.; Mameli, V.; Cara, C.; Musinu, A.; Sangregorio, C.; Niznansky, D.; Xin, H. L.; Vejpravova, J.; Cannas, C. Coupled Hard–Soft Spinel Ferrite-Based Core–Shell Nanoarchitectures: Magnetic Properties and Heating Abilities. *Nanoscale Adv.* **2020**, *2* (8), 3191–3201. https://doi.org/10.1039/D0NA00134A.

(12) Zhang, Q.; Castellanos-Rubio, I.; Munshi, R.; Orue, I.; Pelaz, B.; Gries, K. I.; Parak, W. J.; Del Pino, P.; Pralle, A. Model Driven Optimization of Magnetic Anisotropy of Exchange-Coupled Core-Shell Ferrite Nanoparticles for Maximal Hysteretic Loss. *Chem. Mater.* **2015**, *27* (21), 7380–7387. https://doi.org/10.1021/acs.chemmater.5b03261.

(13) Angelakeris, M.; Li, Z.-A. A.; Hilgendorff, M.; Simeonidis, K.; Sakellari, D.; Filippousi, M.; Tian, H.; Van Tendeloo, G.; Spasova, M.; Acet, M.; et al. Enhanced Biomedical Heat-Triggered Carriers via Nanomagnetism Tuning in Ferrite-Based Nanoparticles. *J. Magn. Magn. Mater.* **2015**, *381*, 179–187. https://doi.org/10.1016/j.jmmm.2014.12.069.

(14) Solopan, S. O.; Nedelko, N.; Lewińska, S.; Ślawska-Waniewska, A.; Zamorskyi, V. O.; Tovstolytkin, A. I.; Belous, A. G. Core/Shell Architecture as an Efficient Tool to Tune DC Magnetic Parameters and AC Losses in Spinel Ferrite Nanoparticles. *J. Alloys Compd.* **2019**, *788*, 1203–1210. https://doi.org/10.1016/j.jallcom.2019.02.276.

(15) Yelenich, O. V.; Solopan, S. O.; Greneche, J. M.; Belous, A. G. Synthesis and Properties MFe2O4 (M = Fe, Co) Nanoparticles and Core–Shell Structures. *Solid State Sci.* **2015**, *46*, 19–26. https://doi.org/10.1016/j.solidstatesciences.2015.05.011.

(16) De Palma, R.; Peeters, S.; Van Bael, M. J.; Van Den Rul, H.; Bonroy, K.; Laureyn, W.; Mullens, J.; Borghs, G.; Maes, G. Silane Ligand Exchange to Make Hydrophobic Superparamagnetic Nanoparticles Water-Dispersible. *Chem. Mater.* **2007**, *19* (7), 1821–1831. https://doi.org/10.1021/cm0628000.